Supporting Information

Optimizing electronic synergy of atomically dispersed dual-metal sites for high-efficiency Oxygen Evolution/Reduction Reaction

Yue Wang, Xueting Feng, Ziang Shang, Xintong Li, Chao Ma, Guanzhen Chen, Ying Zhao, Shaoheng Wu , and Yunhu Han**

1. Methods

Chemicals and reagents. Zinc nitrate hexahydrate ($Zn(NO_3)_2·6H_2O$, 99%), nickel nitrate hexahydrate ($Ni(NO_3)_2·6H_2O$, 99%), methanol and iron acetylacetone ($Fe(acac)_3$, 98%), 2-methylimidazole (2-MeIM, 98%) and RuO_2 were purchased from Adamas. Zinc acetate dihydrate ($Zn(CH_3COO)_2$, 99%), anhydrous ethanol, and potassium hydroxide (KOH) were purchased from Greagent. All reagents were used as received and did not need to be further purified. 20% Pt/C was purchased from Johnson Matthy, UK.

Preparation of Fe/ZIF-8 precursors. Firstly, 5.6 mmol of $Zn(NO_3)_2·6H_2O$ and 22.5 mmol of 2-MeIM were dissolved in 45 mL of methanol, and sonicated for 10 min. Then 0.5 mmol of $Fe(acac)_3$ was dispersed in the above 2-MeIM methanol solution and stirred for 30 min. The two solutions were then mixed and stirred for about 10 min. The liquid became turbid and changed from blood-red to orange-red, indicating the start of Fe/ZIF-8 production. The reaction was further carried out at room temperature for 12 h, centrifuged, washed with anhydrous ethanol, and finally dried under vacuum at 65 ℃ for 8 h.

Preparation of Fe/CN and CN. Appropriate amount of the above synthesized Fe/ZIF-8 precursor powder was placed in a ceramic boat, which was put into a tube furnace and heated to 900 ℃ at a heating rate of 5 ℃ min^{-1} in a flowing Ar atmosphere for 2 h. The sample was then naturally cooled to room temperature and collected. After cooling to room temperature, the sample was collected and the Fe/CN sample was prepared for further use. Appropriate amount of the above synthesized ZIF-8 precursor powder was placed in a ceramic boat and calcined in a tube furnace under the same conditions as the Fe/CN sample to obtain the CN sample for further use.

Preparation of Ni@Fe/CN and Ni@CN. Take 40 mg of the above prepared Fe/CN sample in a small beaker, add 0.2 mmol of $Ni(NO_3)_2·6H_2O$ powder, and then add 30 mL of deionized water to disperse and dissolve the drug. The above mixture was sonicated for more than 60 min to make the Fe/CN sample well dispersed and $Ni(NO_3)_2·6H_2O$ fully dissolved in deionized water. The reaction was further impregnated by stirring for 12 h at room temperature. The sample was centrifuged,

washed with anhydrous ethanol and deionized water, and finally dried under vacuum at 65°C for 8 h. The Ni@CN sample was prepared similarly to the Ni@Fe/CN sample, except that the precursor 40 mg of Fe/CN was replaced by 40 mg of CN, and then impregnated with nickel nitrate in aqueous solution, centrifuged, washed, and dried to obtain the Ni@CN sample for further use.

Preparation of FeNi-CN, Fe-CN and Ni-CN electrocatalysts. An appropriate amount of the above synthesized Ni@Fe/CN powder sample was placed in a ceramic boat, which was placed in a tube furnace and heated to 500°C at a heating rate of 5°C min^{-1} in the atmosphere of a flowing NH_3/Ar mixture, and kept for 100 min for calcination. After the samples cooled to room temperature, the samples were acid washed to neutrality, the sample was collected and labeled as FeNi-CN. Appropriate amounts of the above synthesized Fe/CN and Ni@CN powder samples were placed in a ceramic boat and calcined in a tube furnace under the same conditions as those of the FeNi-CN electrocatalysts, and the samples were labeled as Fe-CN and Ni-CN.

Quasi-solid-state Zn-air battery assembly. In a conventional setup for the solid-state Zn-air battery, a polished zinc foil measuring 2 × 2 cm^2 (with an additional 2 × 2 cm^2 left blank for current collection) was utilized as the anode. Catalysts coated on carbon cloth measuring 2 × 2 cm^2 (with an additional 2 × 2 cm^2 left blank for current collection) were pressed onto the top of a gel polymer to serve as the cathode. Subsequently, two pieces of white breathable tape were employed to seal the device. Regarding the preparation of the catalyst inks, a mixture was created by blending 10 mg of the FeNi-CN catalyst with 985 μL of ethanol and 15 μL of Nafion solution (5 wt.%) through sonication for 30 minutes. In contrast, for the commercial precious metal catalysts (Pt/C: RuO_2 = 1:1, molar ratio), 5 mg of the catalyst and 15 μL of 5 wt.% Nafion solution were dispersed in 985 μL of ethanol using sonication for 30 minutes. The mass loading of the catalysts was determined to be 2.50 mg cm^{-2} for the FeNi-CN-based battery and 1.25 mg cm^{-2} for the Pt/C+RuO_2-based battery. The gel polymer electrolyte was prepared as follows, 4 g of polyvinyl alcohol powder was dissolved in 40 mL of deionized water at 95°C with stirring until a homogeneous and transparent solution was achieved. Subsequently, 4 mL of 18 M KOH was added dropwise over 40 minutes at

95°C with continuous stirring. The solution was then poured into a mold and frozen in a freezer at -20 °C for 2 hours followed by 0°C for 4 hours.

Liquid Zn-air battery assembly. A homemade, uncomplicated alkaline/neutral liquid Zn-air battery configuration was assembled, employing carbon paper coated with the FeNi-CN catalyst as the air cathode, Zn foil as the anode (the thickness is 0.05 mm), 6 M KOH and 0.2 M $Zn(CH_3COO)_2$ as the alkaline electrolyte. The interface area between the catalyst and the electrolyte on the carbon paper was measured at 1 cm^2, with a mass loading of the FeNi-CN catalyst on the carbon paper estimated at approximately 2 mg cm^{-2}. Additionally, a control sample was prepared by mixing Pt/C and RuO_2 at a molar ratio of 1:1. The specific capacity of the battery can be calculated using the equation:

Specific Capacity = [Discharge Current (mA) × Time (h)]/ Weight of consumed Zn (g)

Energy Density = {[Current (mA) × Time (h)] /Weight of consumed Zn (kg)} ×Discharge

2. Structural characterizations

Scanning electron microscopy (SEM) was performed on a Hitachi S4800 electron microscope with an accelerating voltage of 30 kV. Transmission electron microscopy (TEM) was performed on a Hitachi H-800 microscope. The prepared catalysts were characterized by high resolution transmission electron microscopy (HR-TEM) as well as high angle annular dark field energy dispersive spectroscopy (HAADF-EDS, JEOL-2100FFETEM, operating voltage 200 kV). Powder X-ray diffractometry (PXRD) experiments were performed using a Rigaku RU-200b X-ray powder diffractometer with Cu Kα rays (λ = 1.5406 Å), 2° min^{-1}. Raman spectra were collected on a Horiba JOBIN YVON US/HR800 UV-type high-performance micro-Raman spectrometer system with a laser wavelength of 632.8 nm. X-ray photoelectron spectroscopy (XPS) analysis was performed using a ULVAC PHI Quantera microscope analyzer.

3. Electrochemical measurements

Scan rate of 50 mV/s with a suitable potential range, and LSV plots were recorded at a scan rate of 10 mV/s with a suitable potential range. Tafel plots were obtained from the transformation of LSV test curves, and the kinetic current densities and Koutecky-Levich (K-L) plots were obtained on the basis of the following equations:

$$\frac{1}{J}=\frac{1}{J_k}+\frac{1}{J_L}=\frac{1}{Bw^{1/2}}+\frac{1}{J_k}$$

$$B = 0.62nFC_0D_0^{2/3}V^{-1/6}$$

where J is the test current, J_k and J_L are the kinetic and limiting currents, w is the angular velocity of the disk, n is the number of electron transfers, F is the Faraday's constant (96485 C mol^{-1}), C_0 is the volumetric concentration of O_2 (1.2×10^{-6} mol cm^{-3}), and D_0 is the kinematic viscosity of the electrolyte (0.01 cm^2 s^{-1}).

Then, the transferred electron number (n) was calculated with the following equation:

$$n = 4 \times I_d /(I_d + I_r/N_c)$$

and H_2O_2 yield was calculated with the formular of

$$H_2O_2\% = 200\ I_r/N_c/(I_d+I_r/N_c)\%$$

where I_d, I_r and N_c are the disk current, ring current and the collection efficiency of the ring disk electrode (0.424), respectively.

4. Supplementary Figures

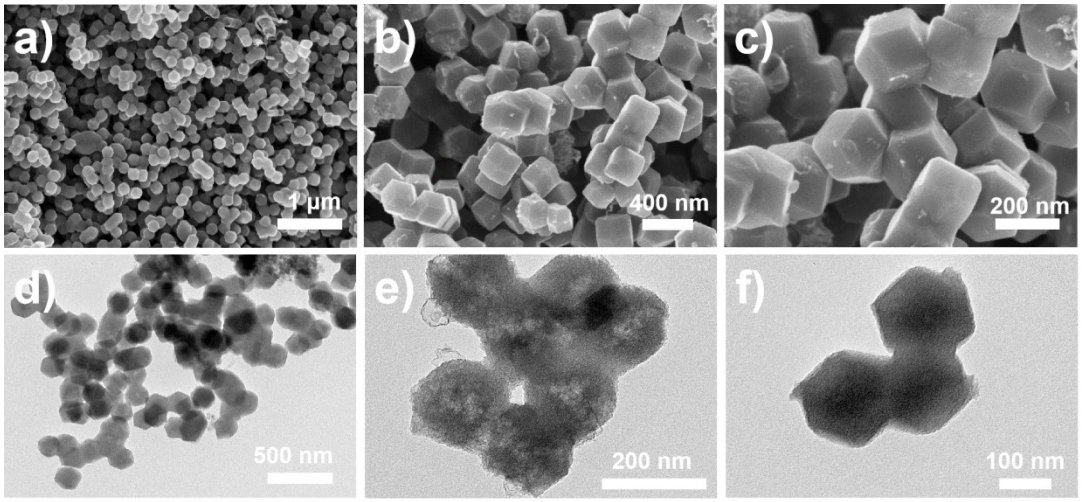

Figure S1. (a-c) SEM images, and (d-f) TEM images of the Fe-CN catalyst.

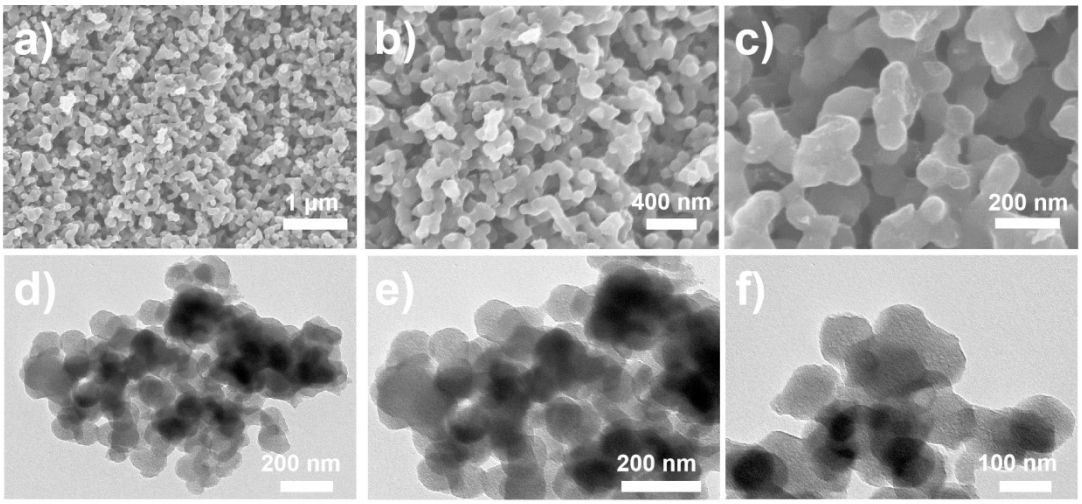

Figure S2. (a-c) SEM images, and (d-f) TEM images of the Ni-CN catalyst.

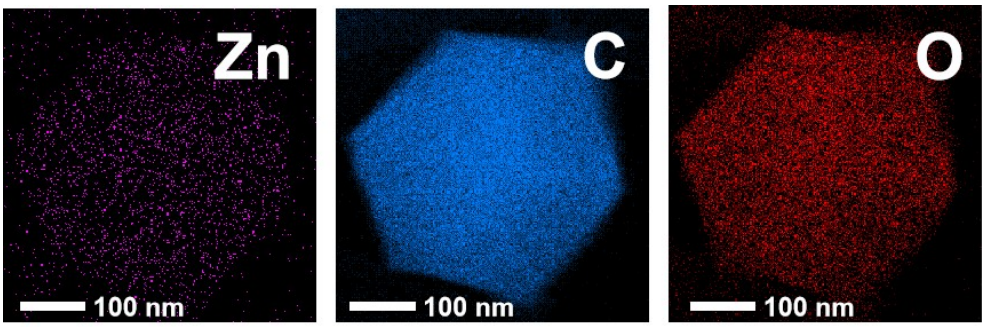

Figure S3. Corresponding EDS elemental maps of Zn, C and O in FeNi-CN catalysts.

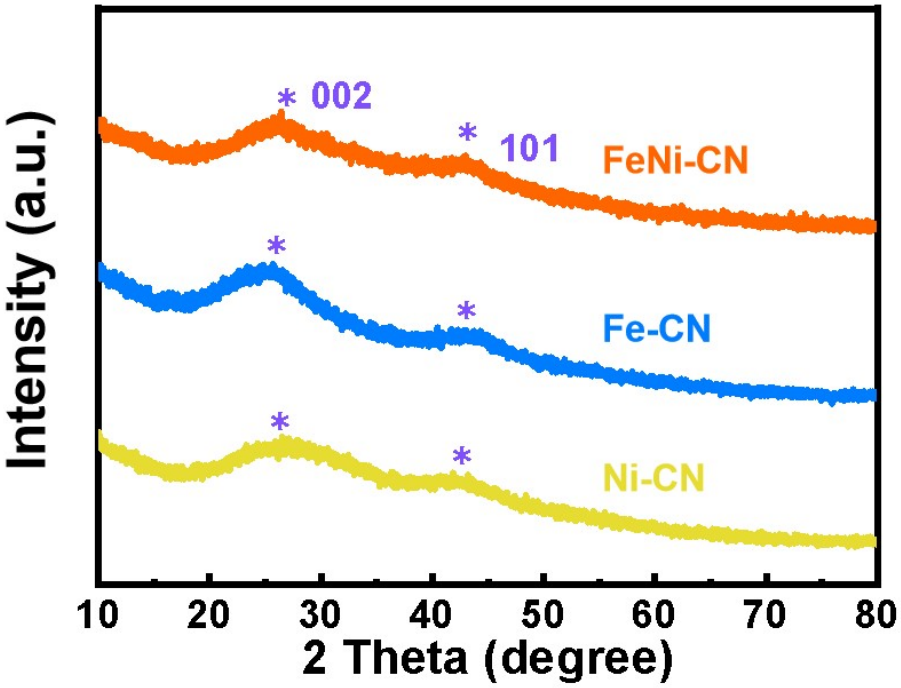

Figure S4. PXRD patterns of the FeNi-CN, Fe-CN and Ni-CN catalysts.

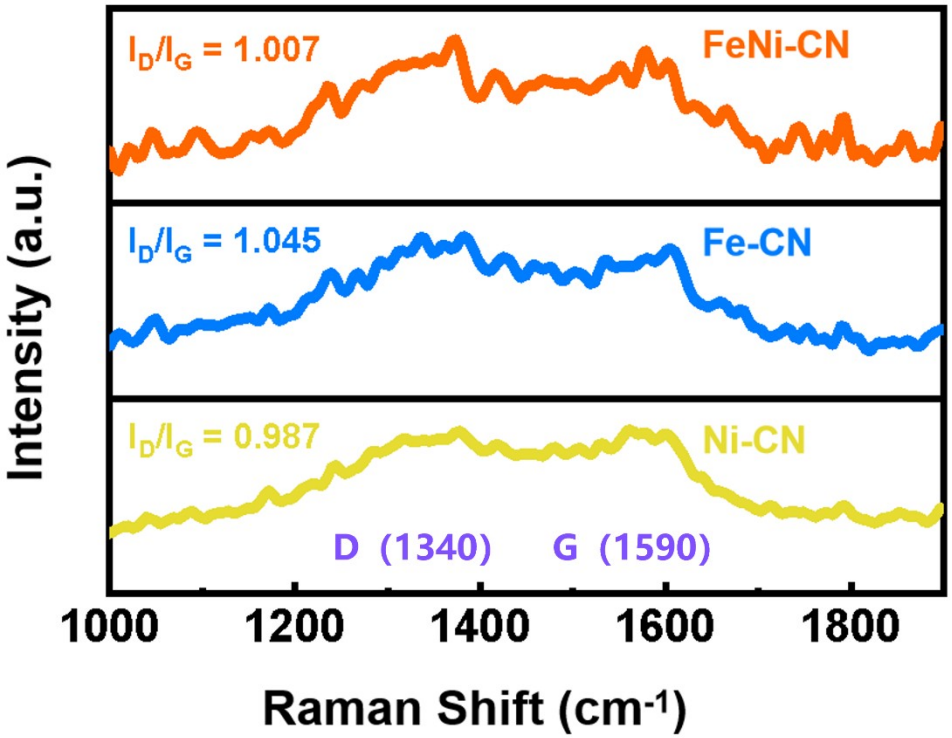

Figure S5. Raman spectra of FeNi-CN, Fe-CN and Ni-CN catalysts.

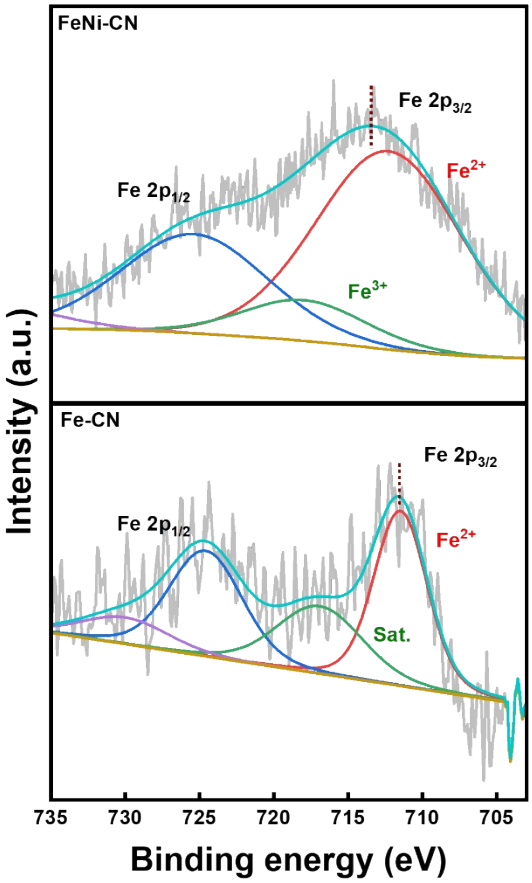

Figure S6. Fe 2p spectra of FeNi-CN and Fe-CN catalysts.

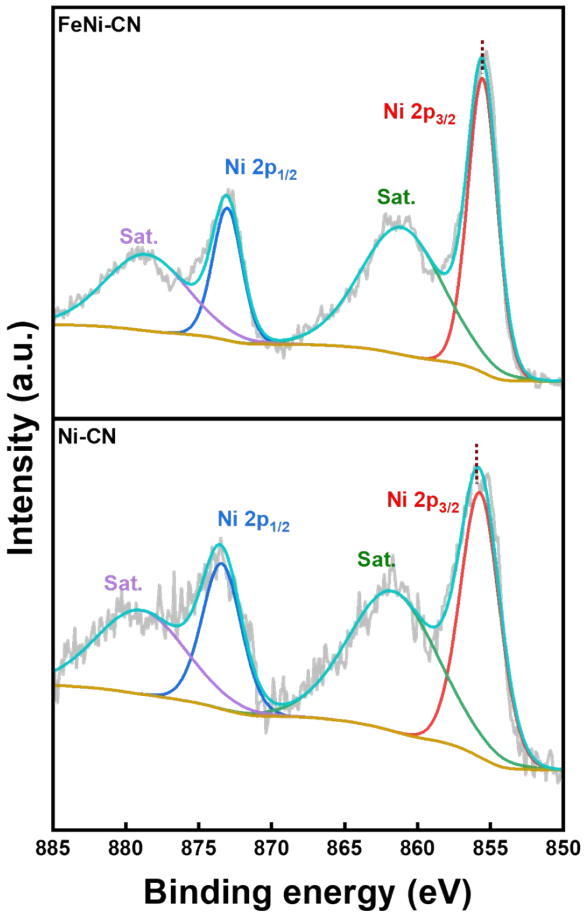

Figure S7. Ni 2p spectra of FeNi-CN and Ni-CN catalysts.

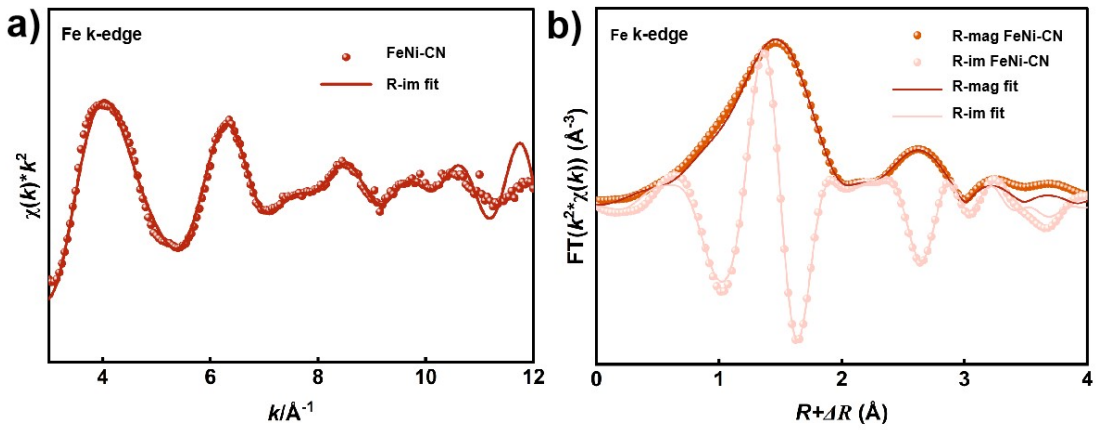

Figure S8. EXAFS fitting curves of Fe K-edge at *k* space for the FeNi-CN catalyst.

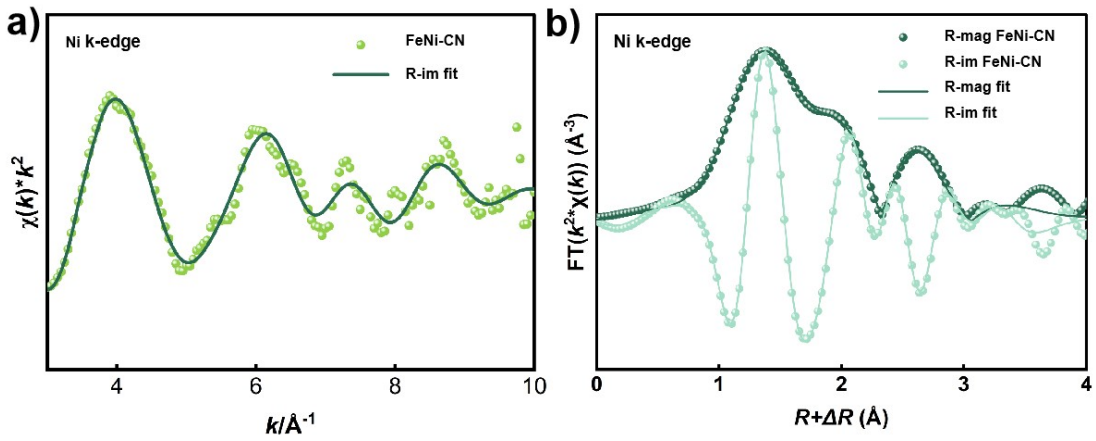

Figure S9. EXAFS fitting curves of Ni K-edge at *k* space for the FeNi-CN catalyst.

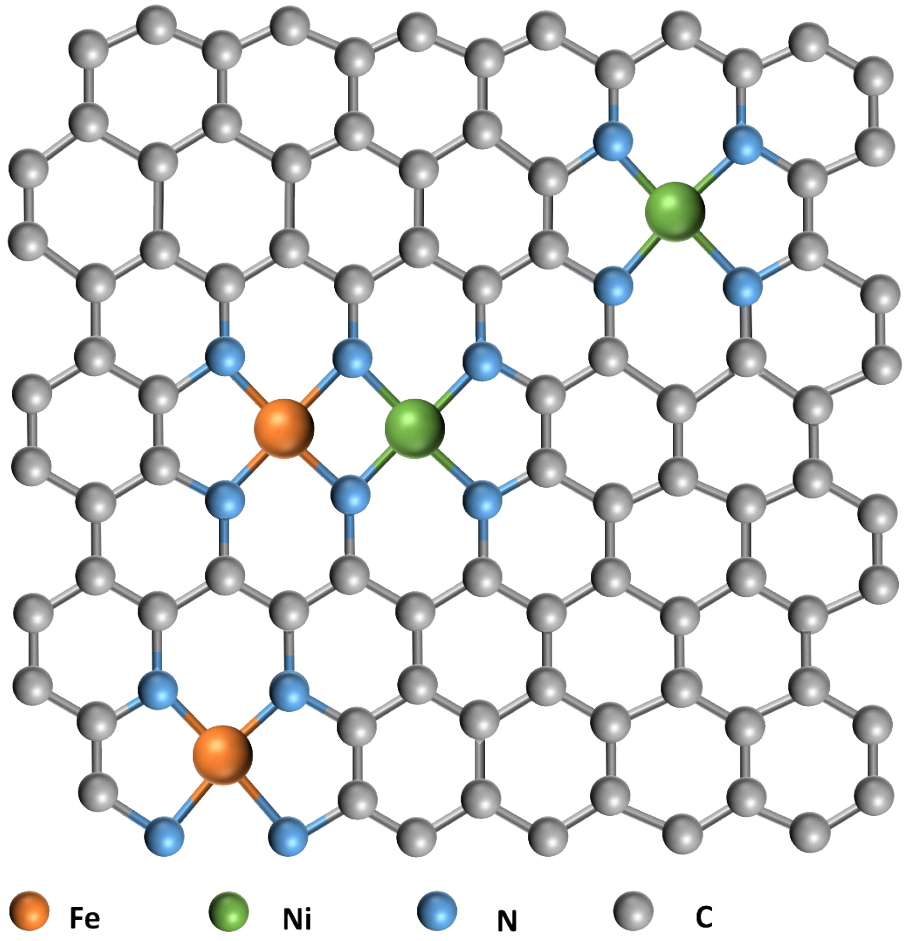

Figure S10. Schematic representation of the atomic structure of the FeNi site.

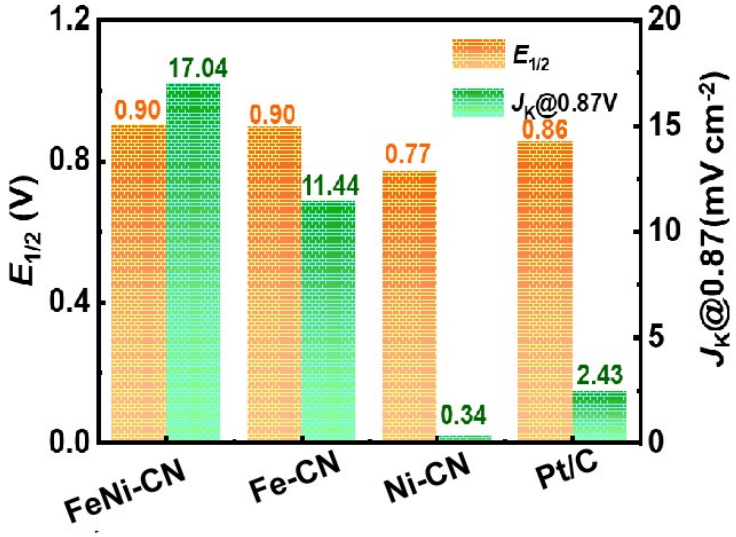

Figure S11. Comparison of $E_{1/2}$ and J_K@0.87V.

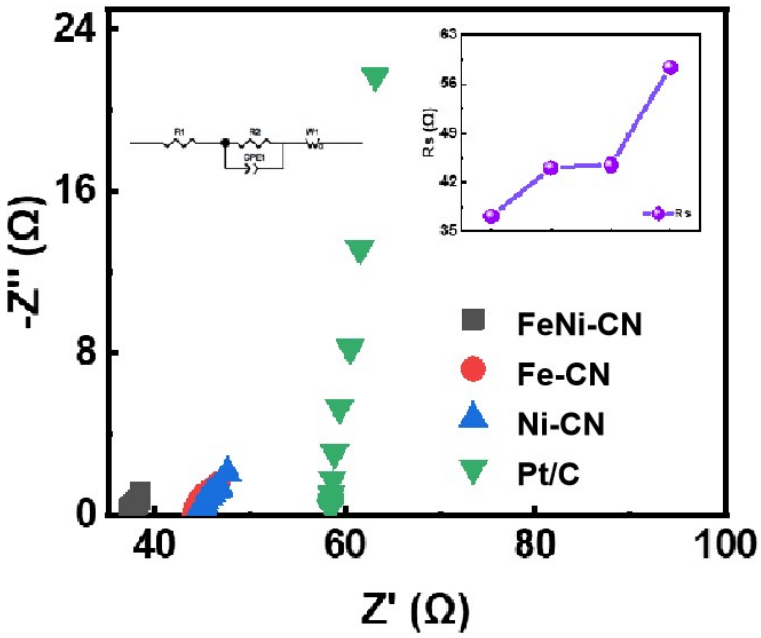

Figure S12. Nyquist plots (insert: Ohm resistance and Circuit model) of the FeNi-CN, Fe-CN, Ni-CN and commercial Pt/C catalysts in O_2-saturated 0.1 M KOH media at 1600 rpm.

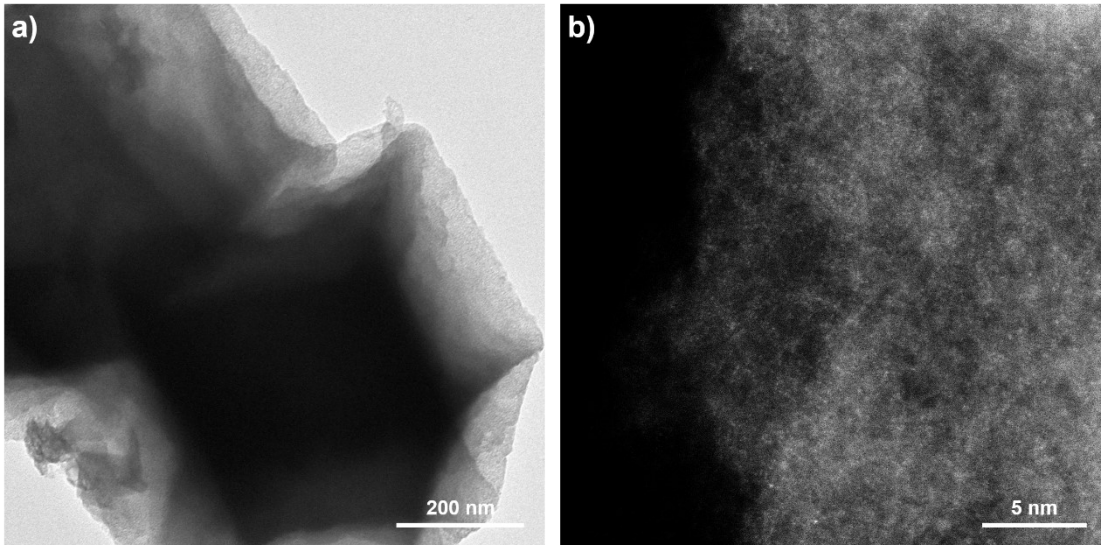

Figure S13. a) TEM image and b) HAADF-STEM image of FeNi-CN.

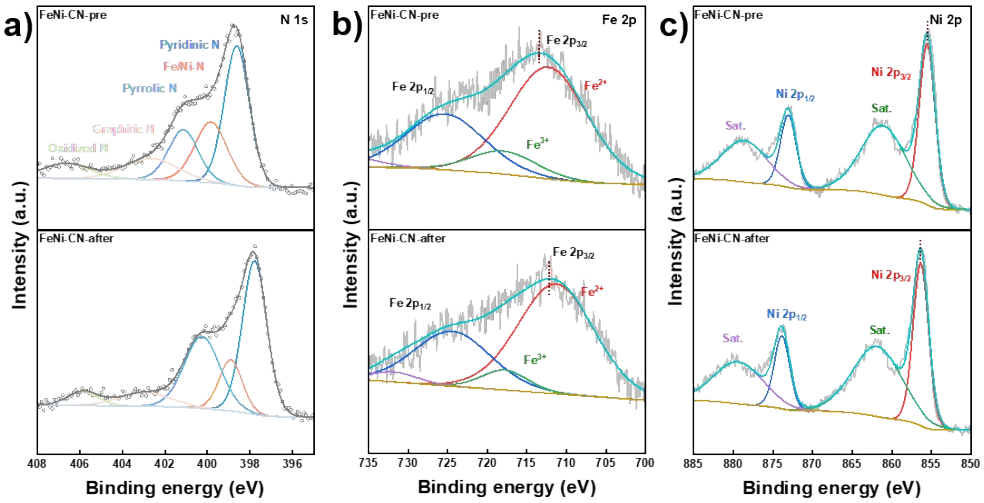

Figure S14. XPS spectra of a) N 1s, b) Fe 2p, and c) Ni 2p for the FeNi-CN before and after stability test. The high-resolution N1s spectra of the catalysts after stability test can be deconvoluted to pyridinic N (397.8 eV), M-Nx (398.9 eV), pyrrolic N (400.2 eV), graphitic N (402.9 eV) and oxidized N (405.8 eV). And the proportion of M-Nx drops from 22.39% to 13.64% after stability test. In the spectra of FeNi-CN after stability test, the Fe and Ni peaks are shifted to lower and higher binding energies, respectively, compared to FeNi-CN.

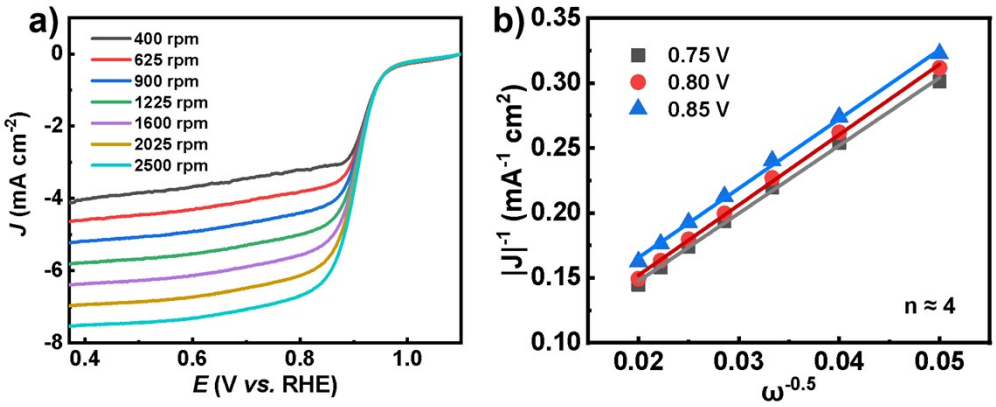

Figure S15. (a) LSV curves at different rotating rates, and (b) Koutecky-Levich (K-L) plots of the FeNi-CN catalyst in O_2-saturated 0.1 M KOH media.

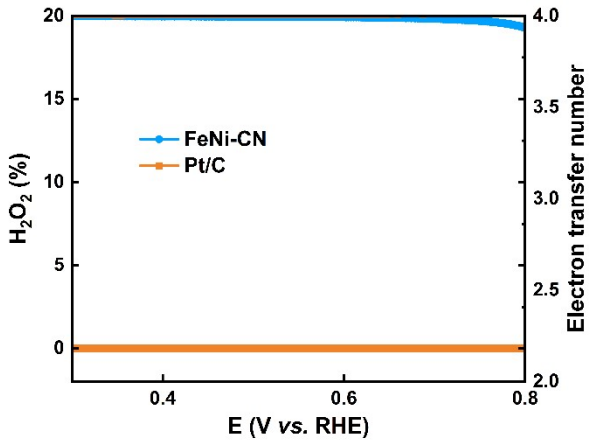

Figure S16. Hydrogen peroxide yield and electron transfer number plots of FeNi-CN and commercial Pt/C catalysts in O_2-saturated 0.1 M KOH solution.

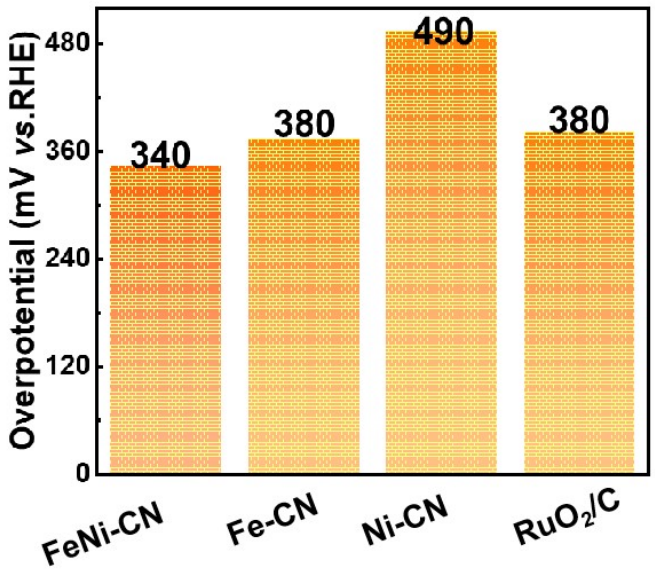

Figure S17. Comparition of overpotential @ 10 mA cm^{-2}.

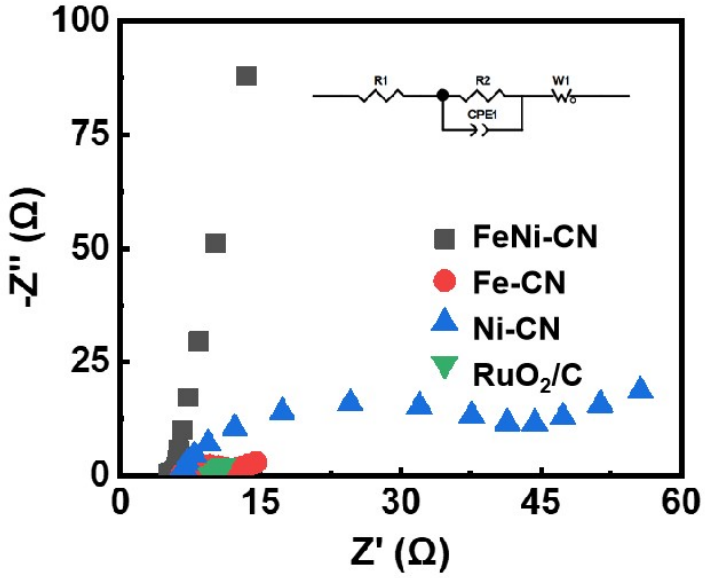

Figure S18. Nyquist plots (insert: circuit model) of the FeNi-CN, Fe-CN, Ni-CN and commercial Pt/C catalysts in N_2-saturated 1 M KOH media at 1600 rpm.

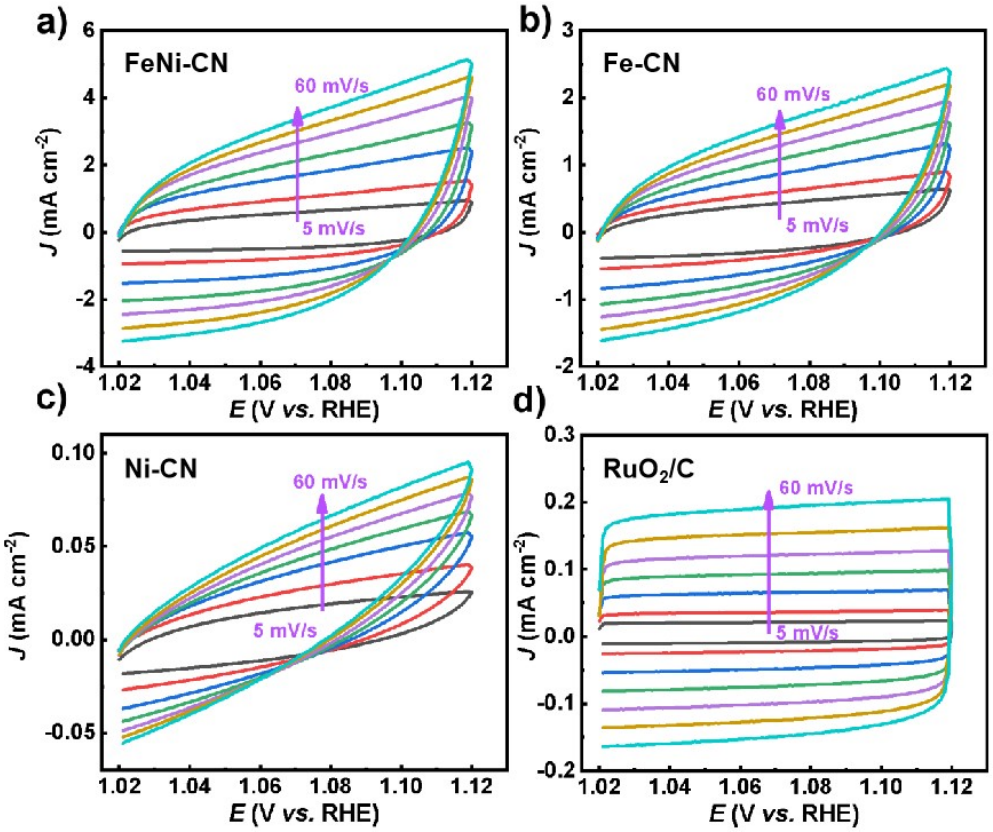

Figure S19. CV curves of the (a) FeNi-CN, (b) Fe-CN, (c) Ni-CN, and (d) RuO_2/C catalysts under different scanning speeds.

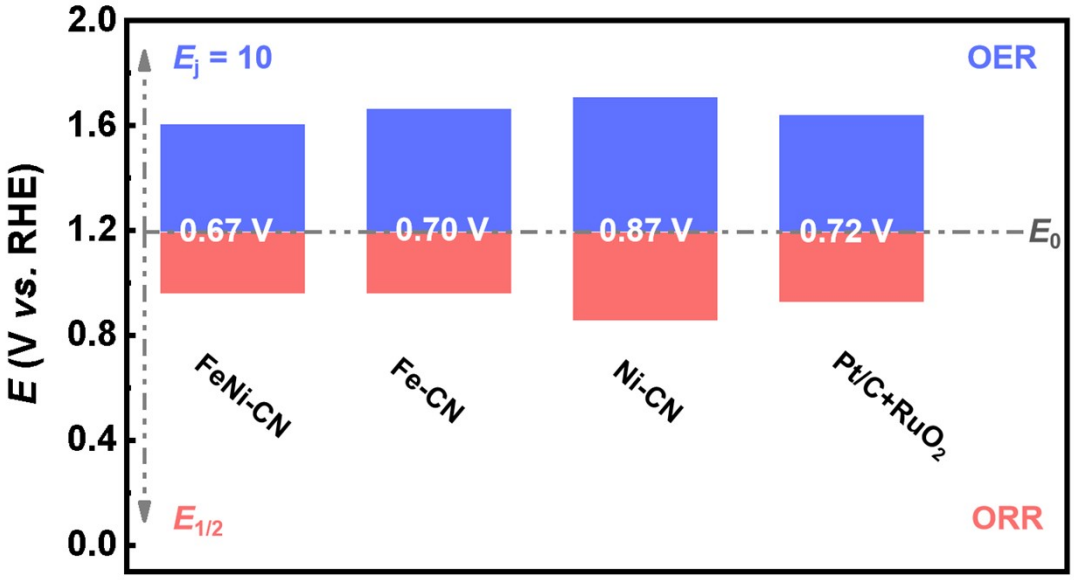

Figure S20. Comparison of the ΔE of the FeNi-CN, Fe-CN, Ni-CN and RuO_2/C catalysts.

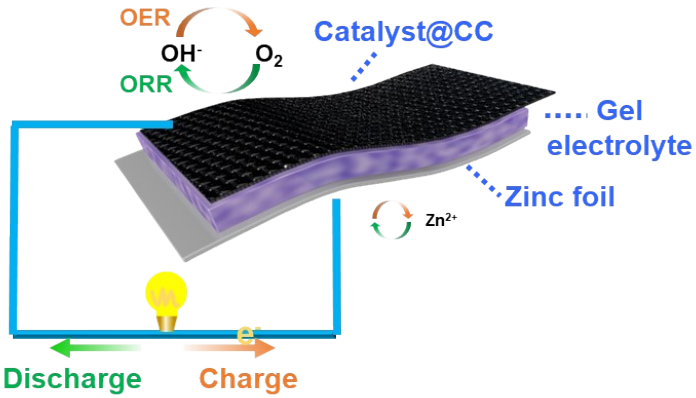

Figure S21. Schematic illustration of a homemade flexible quasi-solid-state alkaline ZAB.

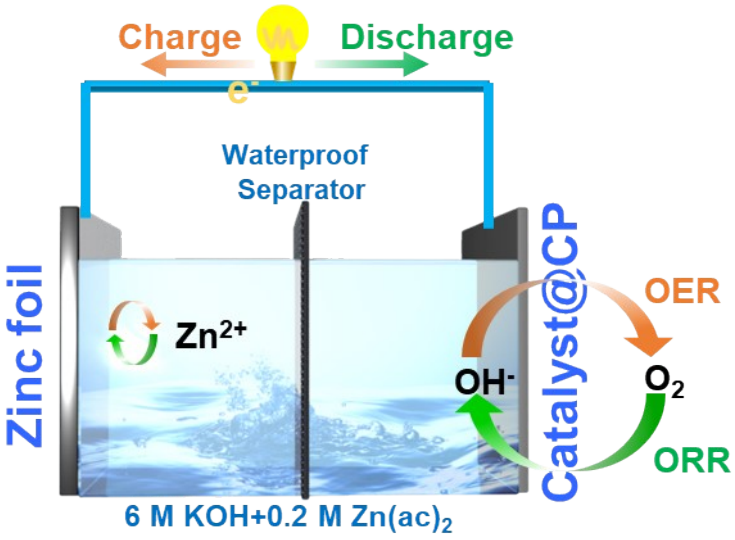

Figure S22. Schematic illustration of a homemade liquid alkaline ZAB.

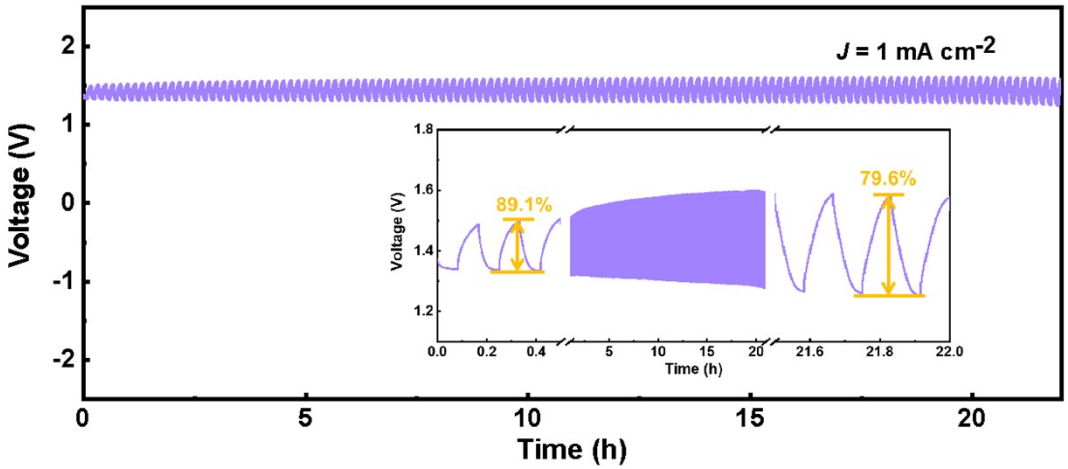

Figure S23. Cycling stability test of flexible quasi-solid-state alkaline ZABs with air cathodes of the FeNi-CN catalyst.

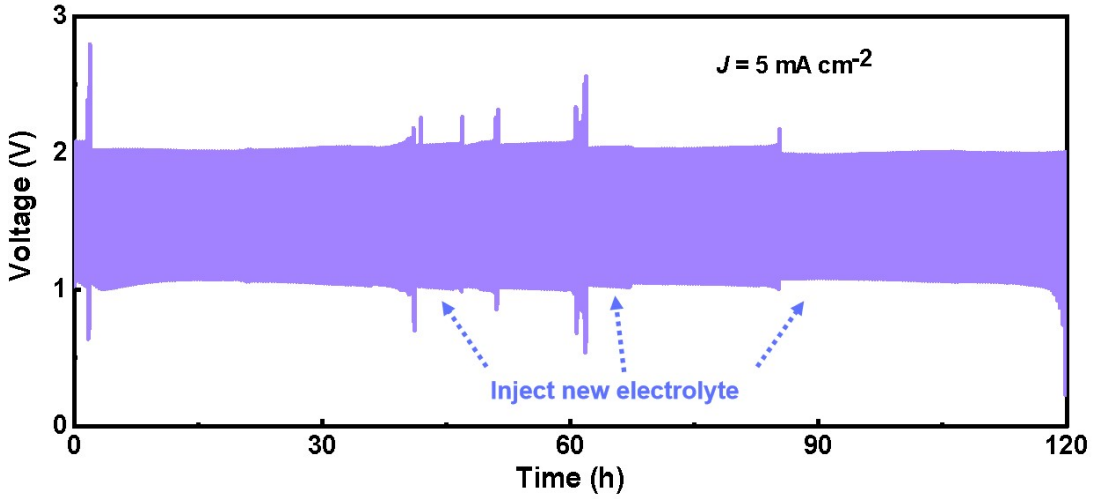

Figure S24. Cycling stability test of liquid alkaline ZABs with air cathodes of the FeNi-CN catalyst.

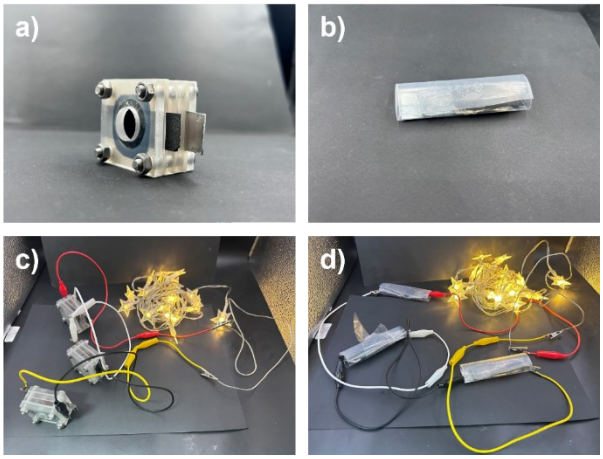

Figure S25. a) Photograph of the liquid alkaline ZABs with air cathodes of the FeNi-CN and Pt/C+RuO_2 catalysts. b) Photograph of the flexible quasi-solid-state ZABs with air cathodes of the FeNi-CN and Pt/C+RuO_2 catalysts. LED strip lit by c) the liquid ZABs in alkaline electrolyte and d) flexible quasi-solid-state ZABs.

Table S1. Content of metal elements in FeNi-CN catalysts.

Sample	Element	Content(wt%)
FeNi-CN	Fe	0.60
	Ni	1.86

Table S2. Structural parameters of FeNi-CN extracted from the EXAFS fitting. (S_0^2=1.0)

Sample	Shell	CN	R (Å)	σ^2 (10^{-3}Å^2)	ΔE_0 (eV)	R-factor
FeNi-CN	Fe-N	4.704±0.276	1.872±0.113	1.08±0.55		
	Fe-N-Ni	1.575±0.361	2.955±0.287	0.17±0.36	-4.917	0.0054
	Fe-N-Fe	0.002±0.734	2.749±1.034	0.03±1.88		
	Ni-N	3.266±0.041	1.958±0.100	0.09±0.08		
	Ni-N-Fe	1.263±0.991	2.973±0.013	0.22±0.62	-4.115	0.0035
	Ni-N-Ni	0.005±1.292	2.964±0.086	0.22±0.08		

S_0^2 is the amplitude reduction factor,
CN is the coordination number,
R is interatomic distance (the bond length between central atoms and surrounding coordination atoms),
σ^2 is Debye-Waller factor (a measure of thermal and static disorder in absorber-scatterer distances),
ΔE_0 is edge-energy shift (the difference between the zero kinetic energy value of the sample and that of the theoretical model),
R-factor is used to value the goodness of the fitting.

Table S3. Summary of the performance of the non-noble metal bifunctional catalysts

Catalysts	$E_{1/2}$ **(V vs. RHE)**	**Tafel slope (mV dec^{-1})**	**Overpotential @ J_{10} / mV**	**Tafel slope (mV dec^{-1})**	**ΔE(V vs. RHE)**	**Ref**
FeNi-CN	0.90	40	340	43	0.67	This work
m-$Fe_{2.04}Ni_{0.66}$@GCFs	0.81	77.5	310	74.6	0.73	[1]
FeN_4B-NiN_4B	0.9	61	388	-	0.718	[2]
NPC-950	0.88	63.7	371	63.5	0.72	[3]
$NiCo_{1.8}Fe_{0.2}O_4$@NCF	0.86	70	270	130	0.64	[4]
CoFe-FeNC	0.876	80.83	296	44.76	0.65	[5]
FeCo–N–C-1.25	0.853	41.75	295	61.18	0.672	[6]
Cu-Co/NC	0.92	63.6	335	83.5	0.645	[7]
PtPdFeCoNi/HOPNC	0.866	53.9	310	88.7	0.674	[8]
Co_4N@d-NCNWs/D	0.83	-	340	65	0.74	[9]
LDH A-$Fe_{SA}Co_{SA}$-$FeCo_{Alloy}$-CNT/NC	0.84	89	330	125.5	0.72	[10]
Fe/I-N-CR	0.915	52.9	329	1.559	0.64	[11]
FeOCo SAD	0.87	117	310	1.654	0.67	[12]

4. References

1. K. Ding, J. Hu, L. Zhao, W. Jin, H. Yu, Y. Liu, Z. Wu, S. Cai, Y. Yang, G. Zou, H. Hou, X. Ji, *Nano Energy*, 2024, **121**, 109270.
2. Z. Wang, R. Xu, Q. Ye, X. Jin, Z. Lu, Z. Yang, Y. Wang, T. Yan, Y. Liu, Z. Pan, S. J. Hwang, H. J. Fan, *Adv. Funct. Mater.*, 2024, **34**, 2315376.
3. Z. Li, S. Ji, H. Liu, C. Xu, C. Guo, X. Lu, H. Sun, S. Dou, S. Xin, J. H. Horton, C. He, *Adv. Funct. Mater.*, 2024, **34**, 2314444.
4. Y. Liu, L. Zhou, S. Liu, S. Li, J. Zhou, X. Li, X. Chen, K. Sun, B. Li, J. Jiang, H. Pang, *Angew. Chem., Int. Ed.*, 2024, **63**, e202319983.
5. S. Zhang, J. Yang, L. Yang, T. Yang, Y. Liu, L. Zhou, Z. Xu, X. Zhou, J. Tang, *Appl. Catal., B*, 2024, **359**, 124485.
6. H. Liu, J. Huang, K. Feng, R. Xiong, S. Ma, R. Wang, Q. Fu, M. Rafique, Z. Liu, J. Han, D. Hua, J. Li, J. Zhong, X. Wang, Z. Zhao, T. Yao, S. Jiang, P. Xu, Z. Zhang, B. Song, *Angew. Chem., Int. Ed.*, 2024, e202419595.
7. Z. Li, S. Ji, C. Wang, H. Liu, L. Leng, L. Du, J. Gao, M. Qiao, J. H. Horton, Y. Wang, *Adv. Mater.*, 2023, **35**, 2300905
8. M. Xie, Y. Lu, X. Xiao, D. Wu, B. Shao, H. Nian, C. Wu, W. Wang, J. Gu, S. Han, M. Gu, Q. Xu, *Adv. Funct. Mater.*, 2024, **34**, 2414537
9. C. Zhang, N. Huang, Z. Zhai, L. Liu, B. Chen, B. Yang, X. Jiang, N. Yang, *Adv. Energy Mater.*, 2023, **13**, 2301749.
10. W.-X. Hong, W.-H. Wang, Y.-H. Chang, H. Pourzolfaghar, I. H. Tseng, Y.-Y. Li, *Nano Energy*, 2024, **121**, 109236.
11. M. Du, B. Chu, Q. Wang, C. Li, Y. Lu, Z. Zhang, X. Xiao, C. Q. Xu, M. Gu, J. Li, H. Pang, Q. Xu, *Adv. Mater.*, 2024, **36**, 2412978
12. Q. Zhou, W. Xue, X. Cui, P. Wang, S. Zuo, F. Mo, C. Li, G. Liu, S. Ouyang, S. Zhan, J. Chen, C. Wang, *Proc. Natl. Acad. Sci.*, 2024, **121**, e2404013121.